

Contents lists available at ScienceDirect

Materialia

journal homepage: www.elsevier.com/locate/mtla



Synchrotron x-ray diffraction and crystal plasticity modeling study of martensitic transformation, texture development, and stress partitioning in deep-drawn TRIP steels



Peijun Hou^a, Yuan Li^a, Wei Zhang^a, Dongchul Chae^b, Jun-Sang Park^c, Yang Ren^c, Yanfei Gao^{a,*}, Hahn Choo^{a,*}

- ^a Department of Materials Science and Engineering, The University of Tennessee, Knoxville, TN 37996, USA
- ^b Stainless Steel Research Group, POSCO Technical Research Laboratory, Pohang, 37859, South Korea
- ^cX-ray Science Division, Argonne National Laboratory, Lemont, IL 60439, USA

ARTICLE INFO

Keywords: Duplex TRIP steel Texture Residual stress Synchrotron x-ray diffraction Crystal plasticity finite element model

ABSTRACT

The micromechanics of the formability of a lean duplex TRIP steel was investigated using Synchrotron X-Ray Diffraction (S-XRD) measurements and Crystal Plasticity Finite Element Modeling (CPFEM). Specifically, the effect of the ferrite phase on the reduction of stress concentrations in the martensite phase and the influence of the austenite texture on the distribution of the martensite phase in the deep-drawn duplex TRIP steel were studied in comparison to a TRIP steel case. A series of deep-drawing processes were carried out to examine the sheet formability at ambient temperature, followed by S-XRD evaluations of the phase fraction, texture, and the residual-stress distributions in the deep-drawn cups. The macroscopic residual stress and its partitioning among constituent phases were studied using both S-XRD and CPFEM. In the deep-drawn TRIP steel, large tensile hoop residual stresses concentrated in the strain-induced α martensite phase, correlating well with the cracking phenomenon observed. Furthermore, the initial austenite texture influenced the martensite transformation kinetics during the deep-drawing process, resulting in a heterogeneous distribution of the martensite phase fractions around the circumference of the deep-drawn cups, which, in turn, caused an orientation-dependent cracking behavior. In the deep-drawn duplex TRIP steel, the tensile hoop residual stresses in the α martensite phase were significantly reduced due to a favorable load partitioning to the ferrite phase, resulting in a better formability.

1. Introduction

The strain localization is one of the critical issues that needs to be addressed for a better formability of alloys during sheet-metal forming processes [1-3]. For example, the strain generated during a sheet-metal forming process concentrates heterogeneously in the form of deformation bands [3-5]. The forming limit diagram, based on the limit strains in the sheet-metal forming process, has been developed as a strain-based failure criterion to evaluate the formability of sheet alloys [6-11]. Numerous mechanistic studies have been reported based on such forming limit diagram [1,12-14]. For example, Ghosh [1] and Kim et al. [12] studied the formability of advanced high-strength steel alloys using numerical analysis and mechanical testing, respectively. These studies show that the limit strain correlates well with the strain rate, strain hardening rate, and fracture elongation. Also, the limit strain can be enhanced by increasing the strain hardening rate, which leads to a delayed onset of necking during the plastic deformation. The method of improving the formability by enhancing the strain hardening rate and ductility was applied in a number of alloy design studies [15-18]. For example, Xie et al. [15] improved the strain hardening rate and ductility of CP800 high-strength steel by optimizing texture components. As a result, the formability was enhanced with the increase in the tensile elongation while maintaining its high strength. Srivastava et al. [16] showed that an optimized heat-treatment condition for a transformation induced plasticity (TRIP) steel could improve the tensile elongation and result in a higher limit strain in the forming limit curve. Accordingly, TRIP steels have gained tremendous interests due to their high tensile strength, strain hardening rate, and tensile ductility [19-24]. However, numerous studies have also reported that the TRIP steels are susceptible to cracking problems during ambient-temperature forming processes [25-28]. Since the cracking problem is often governed by the microstructure and its evolution during the sheet-metal forming process [25,26,29,30], the consideration of the limit strain criterion is not sufficient to provide the basic understanding of the micromechanics controlling the formability of steel alloys with a complex microstructure.

E-mail address: hchoo@utk.edu (H. Choo).

^{*} Corresponding author.

The influence of initial microstructure and its evolution on the stress concentration and hydrogen embrittlement in TRIP steels during forming processes have been studied [27,28,31-34]. For examples, Papula et al. [27] studied the formability of steel alloys with different austenite stabilities during a deep-drawing process using ferrite scope and x-ray diffraction. It was reported that the macroscopic residual stresses increased with the increased content of strain-induced α ' martensite phase and that the martensite phase provided a diffusion path for hydrogen and facilitated the hydrogen embrittlement. On the other hand, Guo et al. [35] and Jung et al. [36] reported that metastable austenitic steel alloys exhibited the cracking phenomenon in their deep-drawn components even when the content of hydrogen was controlled to be less than 0.5 ppm. Similarly, in our recent study [37,38], a TRIP stainless steel alloy exhibited a severe cracking problem during a deep-drawing process at room temperature even when the hydrogen content was kept to a minimum. Even though the TRIP alloy was expected to exhibit a better formability than the austenitic steel counterpart based on the limiting strain criterion with its higher strain hardening rate and tensile ductility, the TRIP case actually showed a much inferior formability.

In general, heterogeneous distribution of the constituent phases in a TRIP or a multiphase steel alloy would result in an interphase stress partitioning and a stress concentration in the brittle martensite phase [20,39]. For example, Tao et al., from their in-situ neutron diffraction study of a ultrafine-grained TRIP alloy, reported that the applied stress was transferred from the austenite phase to the strain-induced α ' martensite phase [20]. Furthermore, the magnitude of accumulated stresses in the strain-induced α ' martensite phase was proposed to be dependent on the phase transformation kinetics, which is influenced by the crystallographic texture. According to a synchrotron x-ray diffraction (S-XRD) study by Cakmak et al. [19], a selective martensitic phase transformation occurred in a TRIP steel, resulting in different martensitic phase transformation rates depending on the formation of deformation textures in the parent austenite phase, as it was observed in a number of other studies [21,40–45].

Therefore, in order to understand the complex relationship between the microstructure and the formability in deep-drawn multiphase alloys, it is important to investigate the role of constituent phases, crystallographic texture, and martensite phase formation in the development of macroscopic residual stresses and the stress partitioning among constituent phases. The high-energy S-XRD measurement has been successfully used for the volumetric mapping of the distributions of phasespecific residual stresses, constituent phase fractions, and texture [45-48]. For example, Gnaeupel-Herold et al. [46] analyzed the distribution of residual stresses in an Al6022 deep-drawn cup and showed that the axial and hoop stresses have non-linear gradients through the thickness and concentrate on the outside surface of the cup wall. Jimenez-Melero et al. [49] used S-XRD to study the texture development and its effect on the martensitic phase transformation in TRIP steel alloys. It was reported that as the <100> pole intensity along the loading direction increased in the austenite phase, the martensitic phase transformation rate increased due to the changes in the critical stress for the phase transformation.

In the current study, we investigated the convoluted effects of constituent phases, crystallographic texture, and martensitic phase transformation on the residual-stress partitioning in deep-drawn TRIP-assisted steel alloys to understand the mechanisms responsible for the cracking behavior. Four stainless-steel alloys are prepared with varying combinations of constituent phases and austenite stability: (1) TRIP SS (TRIP), (2) austenitic SS (A-SS), which is a stable reference of TRIP, (3) duplex TRIP SS (D-TRIP), and (4) duplex SS (D-SS), a stable reference of D-TRIP. The formability of these four alloys was examined using a series of deep-drawing processes. The circumferential distributions of texture and strain-induced α ' martensitic phase fraction were measured using S-XRD near the outside surface at the tip of the deep-drawn cup wall. Moreover, the phase-specific residual strains in the deep-drawn cups were mapped through the thickness and along the height of the cup wall using S-XRD. Furthermore, a series of crystal plasticity finite element

model (CPFEM) simulations were conducted to calculate the residual stresses and compared to the measured data to elucidate the complex load portioning behavior. Finally, the effect of ferrite phase in the D-TRIP steel on the reduction of tensile residual stresses in the martensite phase, the influence of initial austenite texture on the heterogeneous distribution of martensite phase fractions around the circumference of the deep-drawn cups, and their collective influence on the macroscopic cracking behavior and formability in TRIP-assisted steels are discussed.

2. Experimental details

2.1. Stainless steel alloys and deep drawing process

Two key stainless steel (SS) alloys produced in the current study are a TRIP SS (TRIP) and a lean duplex TRIP SS (D-TRIP). The initial TRIP alloy blank has a single-phase, metastable austenitic phase. The D-TRIP alloy blank consists of a metastable austenite phase (70 wt.%) and ferrite phase (30 wt.%). In addition, a stable austenitic SS (A-SS) and a duplex SS (D-SS) (with 73 wt.% austenite and 27 wt.% ferrite phases) were also prepared as non-transforming references for the TRIP and D-TRIP, respectively. The alloy compositions are summarized in Table 1. Note that the hydrogen content was controlled to be less than about 0.3 ppm during the alloy manufacturing. More details on the processing and the microstructure including the phase fractions, grain morphology, grain size, and texture of the alloy plates can be found in [37].

Deep drawing was carried out to examine the sheet formability of the four SS alloys by manufacturing cylindrical cups at ambient temperature. The geometries of deep-drawing tool are: 55 mm inner die diameter with 12 mm shoulder radius and 50 mm outer punch diameter with 6 mm shoulder radius, which are all axisymmetric. The surfaces of deep-drawing tools were lubricated using tallow oil. Several round blanks, with the diameter varying from 90 mm, 95 mm, 100 mm, and 105 mm (with 2 mm thickness), were machined to conduct the deep drawing process with different drawing ratios (DRs), ranging from 1.8 to 2.1. The DR is defined as:

$$DR = \frac{D}{d} \tag{1}$$

where D is the initial blank diameter and d is the outer punch diameter. The punch speed of 100 mm/min and the blank holder force of 10 kN were used during the deep-drawing process.

2.2. Synchrotron x-ray diffraction measurements

High-energy synchrotron x-ray diffraction (S-XRD) measurements were conducted to analyze the distributions of phase fraction and crystallographic texture in the deep-drawn SS cups using beamline 11-ID-C at the Advanced Photon Source (APS), Argonne National Laboratory (ANL). A schematic of measurement locations and the S-XRD setup is presented in Fig. 1. Fig. 1a shows a cup with the axial, radial, and hoop orientations marked. A total of seven diffraction samples were extracted using Electrical Discharge Machining (EDM) from the initial rolling direction (RD) to the transverse direction (TD) locations of the cup at every 15° as shown in Fig. 1b. Then, from each sample, a sliver of 1 mm thickness was extracted using the EDM from the outer surface for the S-XRD measurement, Fig. 1b. These specimens were measured using a transmission scattering geometry as a function of rotation angle around the axial direction from 0° to 90° with 15° interval for a full pole coverage, Fig. 1c. As a result, the circumferential distributions of strain-induced α ' martensite fraction and texture were measured from the near-surface volume at the tip (i.e., rim) of the deep-drawn cups processed with a DR of 2.0. The synchrotron x-ray beam, with a wavelength of 0.11798 Å, was collimated to 500 μ m × 500 μ m. The Fit2D software [50] was used to convert the Debye-Scherrer rings into diffraction patterns, followed by Rietveld refinements using MAUD [51] and E-WIMV algorithm [52]. The pole figures and inverse pole figures were generated using MTEX software [53].

Table 1Stainless steel alloys and their chemical compositions (in weight%, with Fe in balance). The hydrogen concentration is in parts-per-million (ppm).

Alloy designation	С	Si	Mn	Cr	Ni	Cu	N	H_2
TRIP SS (TRIP)	.055	.5	7.0	17.1	4.0	-	.200	.32
Austenitic SS (A-SS)	.051	.5	1.0	17.7	12.1	3.0	.196	.23
Lean duplex TRIP SS (D-TRIP)	.085	.6	6.2	18.9	1.1	2.6	.078	.20
Lean duplex SS (D-SS)	.079	.5	6.0	21.0	3.5	2.5	.080	.30

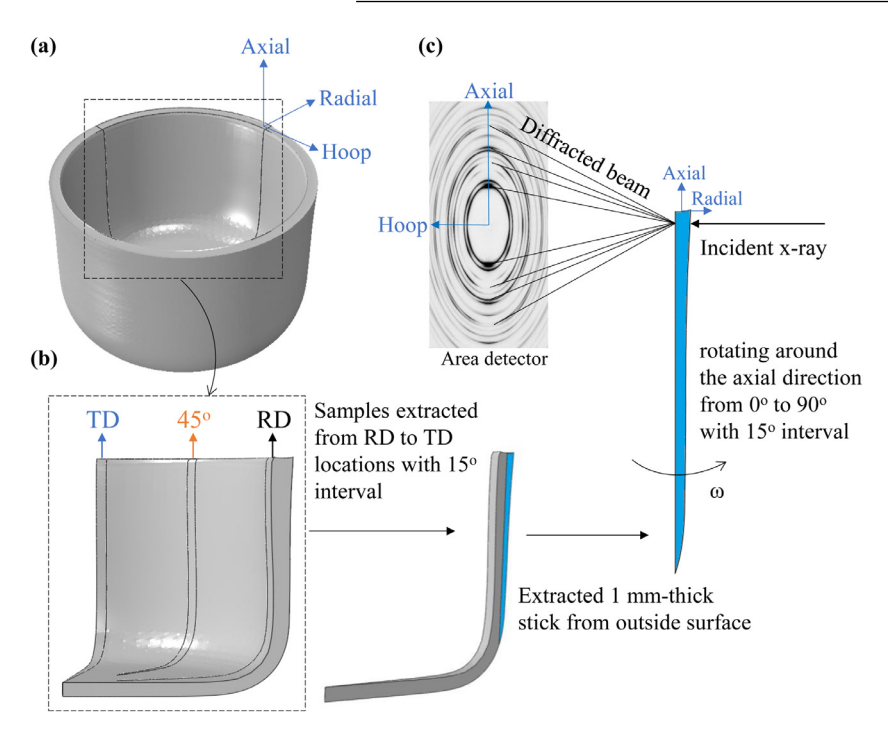


Fig. 1. Schematics of the sample extraction from a deepdrawn cup and scattering setup for the phase fraction and texture measurements using high-energy synchrotron x-ray diffraction (S-XRD) at 11-ID-C beamline at APS. (a) A deepdrawn cup marked with axial, radial, and hoop orientations. (b) Locations of S-XRD sample extraction from a cup in terms of the as-received plate (blank) orientations of RD, 45°, and TD. (c) Transmission x-ray scattering geometry.

The hoop and axial residual strains in the deep-drawn cups (DR of 1.9) were measured at the RD location of the cup using the S-XRD at endstation 1-ID-C, APS, Fig. 2. The scattering volume was defined using conical slits [54,55] to collimate the x-ray beam into 0.05 mm (hoop direction) × 0.05 mm (axial direction) × 0.2 mm (radial direction), allowing strain mapping through the thickness and along the height of the cup wall, Fig. 2b. The wavelengths of the x-ray beam of 0.1711 Å and 0.1597 Å provided diffraction data from the (311) lattice planes of the fcc phase and from the (211) lattice planes of the bcc phases, respectively. About 15 locations were measured at 0.1 mm overlapping interval through the cup wall thickness of about 2.4 mm. Also, 6 locations at 3 mm interval were measured along the cup wall height starting from 0.5 mm below the rim, covering about 50% of the cup wall height. Single-peak fitting was performed using GSAS II software [56] to obtain the d-spacings of (311) austenite and (211) ferrite and α' martensite phases. The lattice strains were then calculated using:

$$\varepsilon_{hkl} = \frac{d_{hkl} - d_{0,hkl}}{d_{0,hkl}} \tag{2}$$

where $d_{0,hkl}$ and d_{hkl} are the measured interplanar spacings for the stress-free and the stressed states, respectively. $d_{0,hkl}$ for each alloy cup was measured using the corresponding as-received alloy plate. The phase-specific residual stress was calculated according to Hooke's law with the assumption of plane-stress condition (i.e., radial residual stress is assumed to be zero) [29,31]:

$$\sigma_{hoop} = \frac{E_{hkl}}{1 - v_{hkl}^2} \left(\varepsilon_{hoop}^{hkl} + v_{hkl} \varepsilon_{axial}^{hkl} \right)$$
 (3)

$$\sigma_{axial} = \frac{E_{hkl}}{1 - v_{hkl}^2} \left(\varepsilon_{axial}^{hkl} + v_{hkl} \varepsilon_{hoop}^{hkl} \right) \tag{4}$$

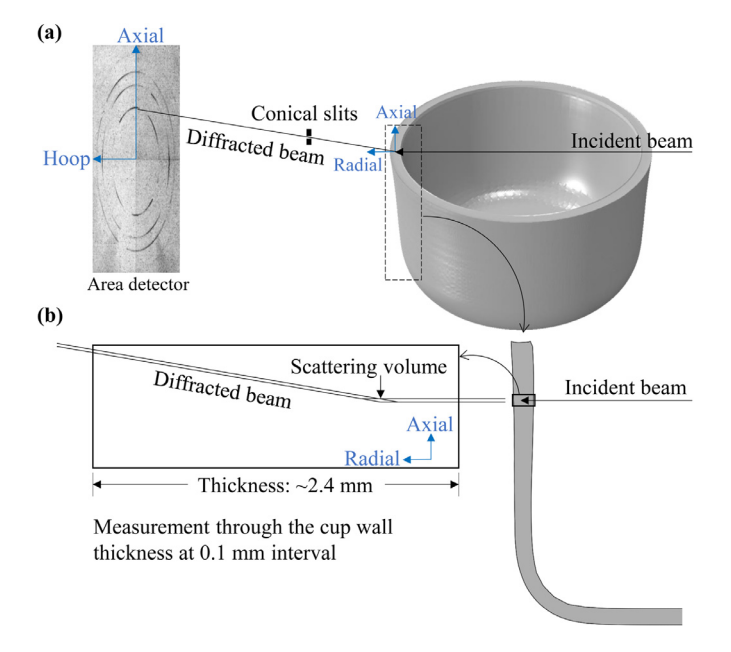


Fig. 2. Schematics of the axial and hoop residual-strain measurement on a deep-drawn cup using S-XRD at 1-ID beamline at APS. (a) Overview of the cup in the x-ray scattering setup showing axial, radial, and hoop orientations, conical slits used on the diffracted beam side, and the area detector. (b) Schematics of a measurement location and a scattering volume during a mapping along the cup wall thickness and height.

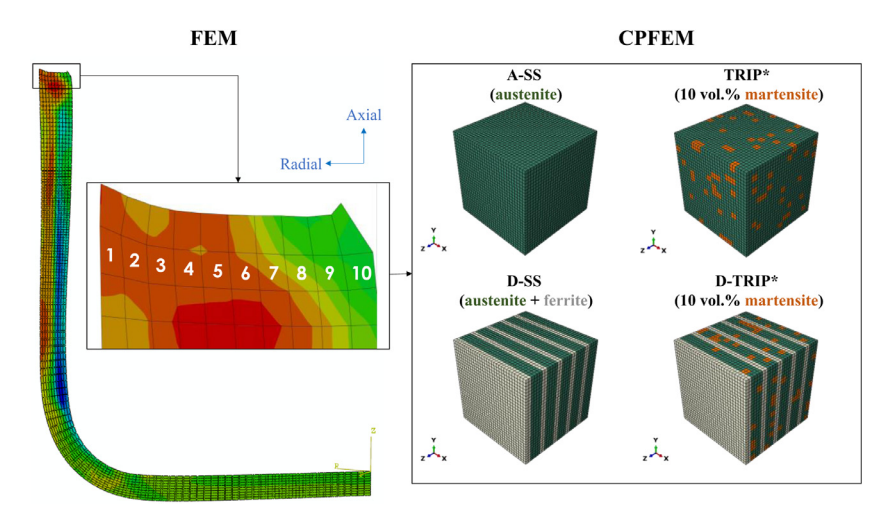


Fig. 3. Illustration of the sequential-coupled crystal plasticity finite element model (CPFEM) simulation for the phase-specific stress development during a deep-drawing process. The initial texture measured using the synchrotron x-ray diffraction (S-XRD) and the lamellar phase structure in the D-SS and D-TRIP* samples are incorporated in the CPFEM simulations.

Table 2a

Macroscopic tensile properties used in the finite element model (FEM) of the deep-drawn A-SS cup: E is the Young's modulus, σ_y is the 0.2% yield stress, UTS is the ultimate tensile strength, ε_u is the uniform elongation, and v is the Poisson's ratio. The data is obtained from a tensile testing along the rolling direction (RD). The measured strain-hardening rate is 1629 MPa up to 25% true strain, which is extrapolated to 62% true strain (ε_z^*) for the FEM.

	E (GPa)	σ_y (MPa)	UTS (MPa)	ε_u^* (%)	ν
A-SS	200	406	1,510	62	0.3

where σ_{hoop} and σ_{axial} are the hoop and axial phase-specific residual stress, and ε_{hoop}^{hkl} and $\varepsilon_{axial}^{hkl}$ are the measured elastic lattice strains in the hoop and axial directions. The diffraction elastic moduli and Poisson's ratios used in the stress calculation are as follows. E_{311} and v_{311} of the austenite phase are 184 GPa and 0.31; and E_{211} and v_{211} of the ferrite phase are 224 GPa and 0.28. These values are obtained based on our previous in-situ neutron diffraction measurements during a series of tensile testing of the as-received alloy plates [37] and Kröner model calculations [57]. The residual stresses in the α ' martensite phase in the deep-drawn cups of TRIP and D-TRIP alloys are calculated based a force-balance method using the residual stresses measured for the austenite and ferrite phases in the deep-drawn A-SS and D-SS cups as references, respectively. In the force balance calculations, changes in the phase fractions due to the martensitic phase transformation are considered.

3. Crystal plasticity finite element modeling

An FEM simulation was conducted to investigate the development of residual stresses generated from the deep-drawing process using ABAQUS/Explicit. The deep-drawing tools (i.e., punch, holder, and die) were set as rigid elements (element type R3D3). The numerical FEM used the same experimental processing conditions mentioned earlier. The steel plate was discretized as 134,170 linear brick elements with one integration point per element (element type C3D8R). To assess the stresses distributed through the thickness of the deep-drawn cup, the thickness of steel plate was discretized as ten elements, Fig. 3. The friction coefficient of each pair-surface interactions was assumed to be 0.05. First, the macroscopic residual stresses in the deep-drawn cup of the single-phase A-SS alloy were simulated using the measured elastic modulus, Poisson's ratio, and plastic deformation behavior, Table 2a. Note that the measured tensile strain-hardening rate $(d\sigma/d\varepsilon)$ of 1,629 MPa (up to 0.25 true strain) was extrapolated to 0.62 true strain during the FEM.

The individual strain histories of the ten through-thickness elements were collected at about $0.5~\mathrm{mm}$ from the tip of the deep-drawn cup

Table 2bPhase fractions used in the crystal plasticity finite element model (CPFEM) presented in volume % (and in weight % in parentheses).

	A-SS	TRIP*	D-SS	D-TRIP*
γ austenite α ferrite α ' martensite	100	90 (94.7) - 10 (5.3)	66.7 (80) 33.3 (20)	56.7 (72.4) 33.3 (21.2) 10 (6.4)

wall of the A-SS cup. Subsequently, they were used as an input to a sequential-coupled crystal plasticity finite element model (CPFEM) along with the initial as-received crystallographic texture measured using the S-XRD. Moreover, the lamellar morphology of the alternating austenite and ferrite phases in the D-SS and D-TRIP alloys was simulated accordingly. The symmetric boundary condition was applied in the CPFEM. A total of 3,375 grains were modeled in each CPFEM, and every grain was composed of 4 elements. The schematic illustration of the CPFEM of the four alloys is summarized in Fig. 3.

Using the CPFEM simulations, the phase-specific stress development and its partitioning during the deep-drawing process were predicted to qualitatively assess the role of the martensite and ferrite phases in the load partitioning. Four specific cases are simulated: (1) A-SS (100 vol.% austenite). (2) TRIP* (90 vol.% austenite and 10 vol.% α ' martensite). (3) D-SS (66.7 vol.% austenite and 33.3 vol.% ferrite), and (4) D-TRIP* (56.7 vol.% austenite, 33.3 vol.% ferrite, and 10 vol.% α ' martensite). The A-SS and D-SS cups were modeled as references for their TRIP counterparts. Moreover, to study the influence of the martensite formation and to compare its effect in TRIP* and D-TRIP*, 10 vol.% α ' phase was added homogenously within the austenite matrix in models of A-SS and D-SS. The constituent phase fractions used in these models are summarized in Table 2b. Note that the * in TRIP* and D-TRIP* simulation sample designations indicates that the current CPFEM result shows a snapshot of the TRIP and D-TRIP behavior with 10 vol.% martensite rather than simulating in-situ formation of the martensite phase.

The finite-element implementation is performed using the user-defined material (UMAT) subroutine in ABAQUS [58]. The CPFEM is based on the classic crystal plasticity theory [59–61], which is briefly outlined here. According to the Taylor-type crystal plasticity, the plastic strain rate is determined as a linear superposition of the slip strain rates of all activated slip systems:

$$\dot{\mathbf{F}}^p \mathbf{F}^{p-1} = \sum_{\alpha=1}^{N_{slip}} \dot{\gamma}^{(\alpha)} \mathbf{s}^{(\alpha)} \otimes \mathbf{m}^{(\alpha)}$$
 (5)

where F^p is the plastic deformation gradient, N_{slip} is the total number of activated slip systems, $\dot{\gamma}^{(\alpha)}$ is the slip rate of the α_{th} slip system, $s^{(\alpha)}$ and $m^{(\alpha)}$ denote the slip direction and slip plane normal, and \otimes represents

Table 2c

Elastic constants (C_{11} , C_{12} , and C_{44}), the initial hardening modulus (h_0), the initial slip strength (τ_0), the saturated slip strength (τ_s), and the latent hardening parameter (q) used in the crystal plasticity finite element model (CPFEM) simulation of the deep-drawing behavior of the four alloy cases, i.e., A-SS, TRIP*, D-SS, and D-TRIP*. The isotropic behavior with perfect plasticity is assumed to simulate the α ' martensite phase in CPFEM.

A-SS and TRIP*							
γ austenite	C ₁₁ (GPa)	C ₁₂ (GPa)	C ₄₄ (GPa)	h ₀ (MPa)	τ ₀ (MPa)	τ _s (MPa)	q
	217.6	138.7	112.7	400	120	300	1.0
α' martensite	E (GPa) 200	ν 0.3	σ _y (MPa) 2,000				
D-SS and D-TRIP*							
	C ₁₁ (GPa)	C ₁₂ (GPa)	C ₄₄ (GPa)	h ₀ (MPa)	τ ₀ (MPa)	τ _s (MPa)	q
γ austenite α ferrite	217.6 231.4	138.7 134.7	112.7 116.4	400 200	60 265	350 600	1.0 1.0
α ' martensite	E (GPa) 200	ν 0.3	σ_y (MPa) 2,000				

the tensor product of the two vectors. The slip rate is given according to the power law relationship of the resolved shear stress $\tau^{(\alpha)}$:

$$\dot{\gamma}^{(\alpha)} = \dot{\gamma}_0 \left| \frac{\tau^{(\alpha)}}{g_{\text{flow}}^{(\alpha)}} \right| \text{sgn}(\tau^{(\alpha)}) \tag{6}$$

where $\dot{\gamma}_0$ is the characteristic strain rate and $g^{(a)}_{\rm flow}$ is the flow strength of the $\alpha_{\rm th}$ slip system. {111}<110> and {110}<111> slip systems are applied in the CPFEM for the fcc and bcc phases, respectively. The hardening law is described based on the Peirce-Asaro-Needleman model [60]:

$$\dot{g}_{\text{flow}}^{(\alpha)} = \sum_{\beta} h_{\alpha\beta} \left| \dot{\gamma}^{(\beta)} \right| \tag{7}$$

where $h_{\alpha\beta}$ is latent hardening moduli, which is expressed as:

$$h_{\alpha\beta} = h(\gamma) \left[q + (1+q)\delta_{\alpha\beta} \right] \tag{8}$$

$$h(\gamma) = h_0 \operatorname{sech}^2 \left| \frac{h_0 \gamma}{\tau_s - \tau_0} \right| \tag{9}$$

where γ is the total slip strain, h_0 is the initial hardening modulus, τ_0 is the initial slip strength, τ_s is the saturated slip strength, q is the latent hardening parameter, and $\delta_{a\beta}$ is the Kronecker delta.

The hkl-specific lattice strain of grains, where the grain <hkl> directions are within 5 degrees with respect to the scattering vector, is expressed as:

$$\varepsilon_{hkl} = \frac{\sum_{1}^{N} \int \varepsilon_{ij}^{\text{elastic}} q_{i} q_{j} d\Omega_{N}}{\sum_{1}^{N} \int d\Omega_{N}}$$
(10)

where N is the number of grains, q_i is the component of scattering vector, and $\Omega_{\rm N}$ denotes the volume of individual grain. $\varepsilon_{ij}^{\rm elastic}$ is the Lagrange-Green strain:

$$\varepsilon_{ij}^{\text{elastic}} = \frac{1}{2} \left(F_{ik}^{\text{e}} F_{kj}^{\text{e}} - \delta_{ij} \right) \tag{11}$$

where F_{ii}^e is the elastic deformation gradient.

The elastic constants (C_{11} , C_{12} , and C_{44}), the initial hardening modulus (h_0), the initial slip strength (τ_o), the saturated slip strength (τ_s), and the latent hardening parameter (q) used in the current CPFEM are obtained from the lattice strain data measured using in-situ neutron diffraction experiments. The isotropic behavior with perfect plasticity is used to simulate the α ' martensite phase in the CPFEM. The yield stress of the α ' martensite phase is assumed to be 2,000 MPa based on a recent neutron diffraction study on a TRIP steel [43]. These parameters are summarized in Table 2c. More details on the tensile properties and the lattice strain evolutions measured during the tensile testing of the four as-received alloys can be found in [37].

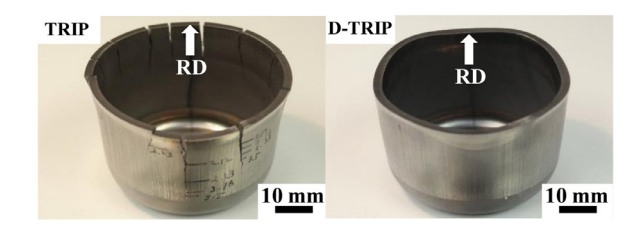


Fig. 4. Deep-drawn cups of TRIP and D-TRIP alloys processed with the DR of 2.1. Several cracks are visible in the TRIP cup, while the D-TRIP cup is crackfree. The RD of the alloy plate is marked with an arrow.

4. Results

4.1. Cracking behavior and the alloy design strategy

The formability of the four SS alloys are studied by conducting a series of ambient-temperature deep-drawing processes and observing the cracking phenomenon under various DRs ranging from 1.8 to 2.1. Of the four alloy cases studied, only the TRIP alloy exhibited macroscopic cracks, while A-SS, D-SS, and D-TRIP cases did not show any visible cracks. The deep-drawn cup of the TRIP alloy formed 0, 1, 4, and 12 longitudinal cracks along the cup height for the DRs of 1.8, 1.9, 2.0, and 2.1, respectively, indicating a relatively poor formability. Fig. 4 shows the TRIP and D-TRIP cups (2.1 DR). Several cracks are clearly visible on the TRIP cup. In contrast, the D-TRIP cup did not exhibit any cracks, exhibiting a better formability. The cracks, which typically initiated on the outside surface at the rim, propagated from the outside surface to inside surface and subsequently propagated down vertically along the cup height. Fig. 5 presents the changes in the crack length in the TRIP cup (2.1 DR) measured as a function of time from the drawing process. Moreover, the crack growth behavior is shown for several cracks located around the circumference of the cup wall. The crack growth rate is quite anisotropic in that the cracks near RD grew faster and longer, whereas cracks away from RD and near TD generally grew slower and shorter.

The A-SS alloy is expected to have a good formability. Also, the high-strength, high-strain-hardening TRIP alloy is supposed to perform well during an ambient-temperature forming process owing to its relatively high tensile strength and ductility. Combined with the much-reduced nickel content, the TRIP alloy should offer a cost-effective, high-performance alloy potentially replacing the A-SS alloy. However, it is evident that the TRIP alloy exhibits a very poor formability under the current deep-drawing conditions. Hence, the current study aims to investigate the effectiveness of a duplex microstructure of D-TRIP on improving the formability of the TRIP alloy, while maintaining the nickel

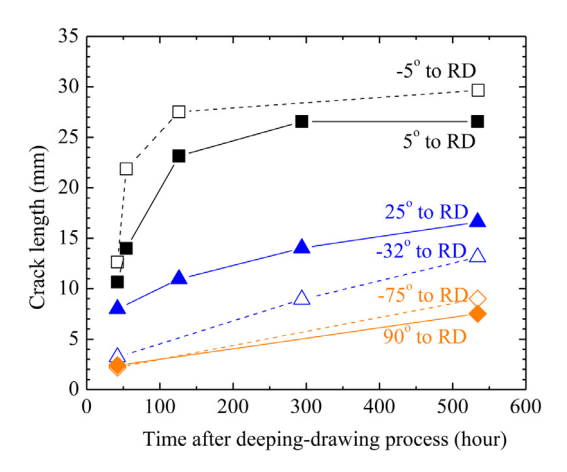


Fig. 5. Changes in the crack lengths over time after the deep drawing of the TRIP alloy cup (2.1 DR). Various cracks around the circumference of the cup wall are shown as a function of the angle from RD.

content as lean as possible (Table 1). Henceforth, the deep-drawn cups of the four alloys will be critically compared in terms of the effects of the microstructure and texture on the residual stress distribution and their implications on the formability.

4.2. Constituent phases and strain-induced α ' martensite phase distribution in the deep-drawn cups

As designed, the A-SS and D-SS cups, as non-transforming stable references, did not exhibit any phase transformations during the deep drawing, while the TRIP and D-TRIP cups showed significant martensitic phase transformations. Example S-XRD diffraction patterns measured at the rim of the cup (2.0 DR) are presented for four alloys in Fig. 6. The TRIP cup consists of austenite (fcc), α ' martensite (bcc), and

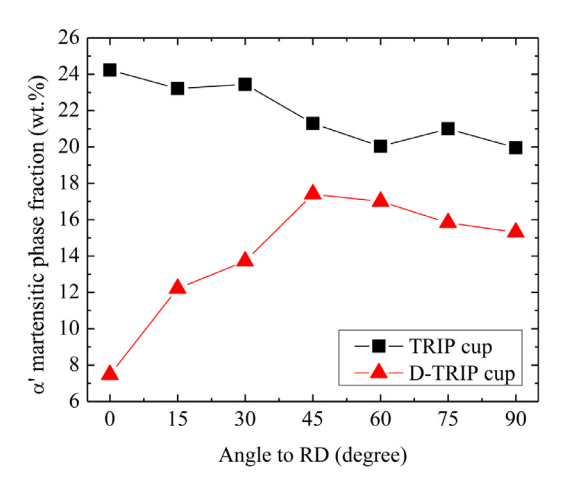


Fig. 7. Variations in the strain-induced α ' martensite phase fraction around the circumference of the TRIP and D-TRIP cups (2.0 DR). The S-XRD measurements were conducted at the outside surface near the rim from RD to TD.

 ε martensite (hcp); whereas its stable counterpart, A-SS cup, has a single austenite phase, Fig. 6a,b. According to the Rietveld refinement analyses, the bcc ferrite phase fraction in the deep-drawn D-SS cup remained constant at the initial value of 27 wt.% measured from the as-received plate, Fig. 6d. In contrast, the bcc phase fraction in the D-TRIP cup is significantly higher than the initial condition (30 wt.% bcc) reflecting a substantial martensitic phase transformation occurred during the deep drawing, Fig. 6c.

More interestingly, there were measurable variations in the α ' fractions around the circumference of the TRIP and D-TRIP cups near the rim, Fig. 7. The distribution of the α ' fraction is heterogeneous in both TRIP and D-TRIP cups likely due to a non-uniform plastic deformation during the deep-drawing process. The α ' fraction is generally higher in

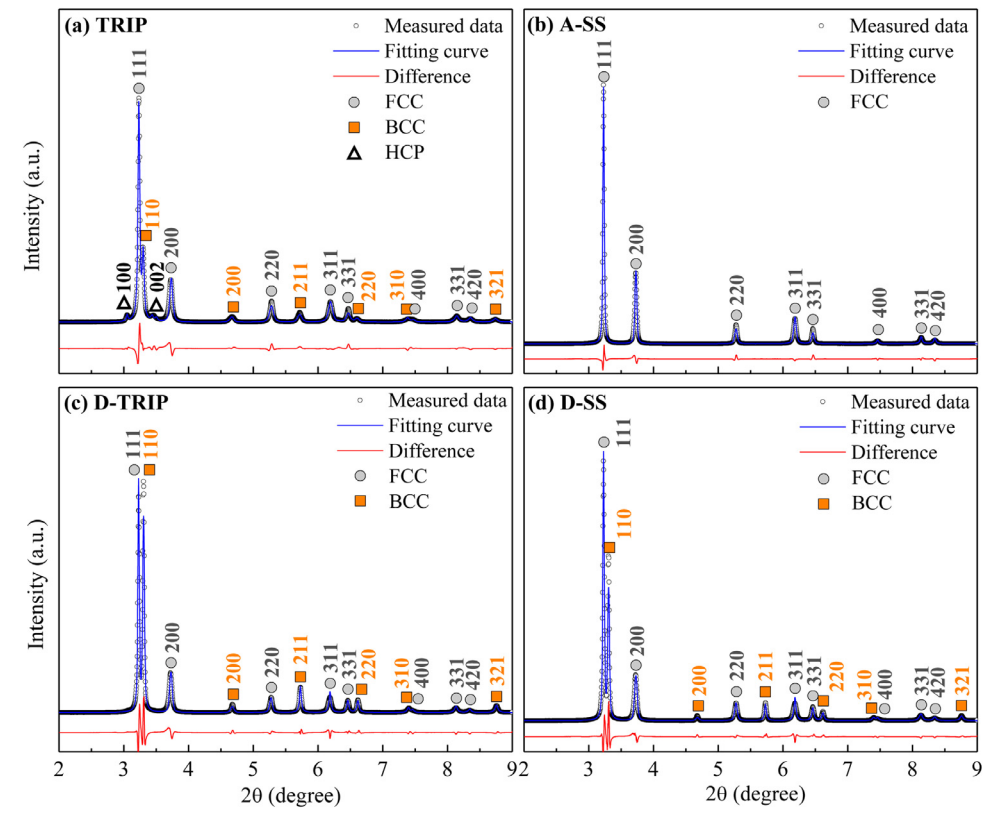


Fig. 6. Synchrotron x-ray diffraction patterns measured from the outside surface near the tip of the deep-drawn cup wall (2.0 DR) as shown in Fig. 1. (a) TRIP, (b) A-SS, (c) D-TRIP, and (d) D-SS.

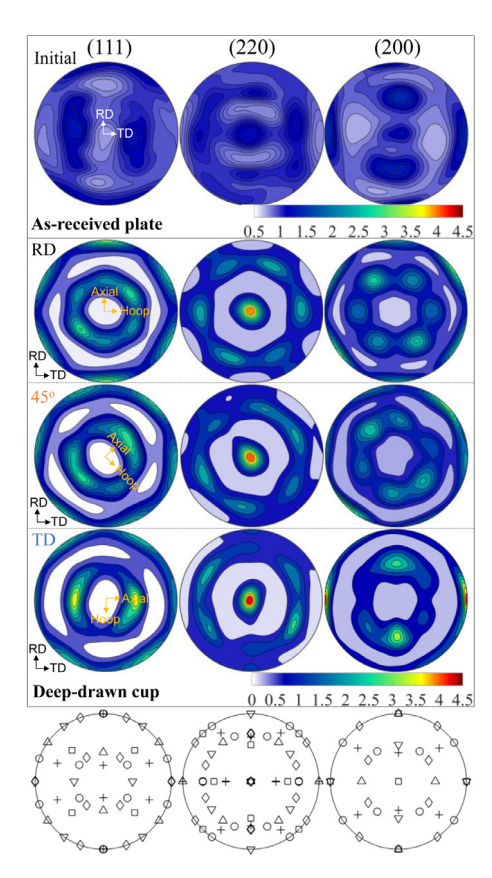


Fig. 8. Texture of A-SS cup (2.0 DR): (111), (220), and (200) pole figures (PFs) of the fcc austenite phase. The PF sets are presented for three locations around the circumference of the cup, i.e., 0° (RD), 45°, 90° (TD) as illustrated in Fig. 1. The RD-ND-TD coordinates of the as-received rolled plate and the axial-radial-hoop coordinates of the deep-drawn cup are presented. Also, PFs of the fcc austenite phase in the as-received A-SS alloy plate and the ideal fcc texture components (Table 3) are also presented as references.

the TRIP cup compared to the D-TRIP cup. In the TRIP cup, the α ' fraction decreases slightly from about 24 wt.% at RD to about 20 wt.% at TD. In contrast, the amount of α ' in the D-TRIP cup increases from 7.5 0wt.% at RD to 17.5 wt.% at 45°, and then decreases slightly to about 15 wt.% at TD. The distribution of α ' phase fractions (Fig. 7) and the crack propagation rates (Fig. 5) observed for the TRIP cup are consistent in that the higher α ' phase fraction correlates with the higher crack propagation rate observed at RD. This suggests that the amount and distribution of strain-induced α ' martensite phase could be closely related to the anisotropic cracking behavior in the deep-drawn cups.

4.3. Texture distribution in the deep-drawn cups

The crystallographic texture was analyzed using the pole figure (PF) measured using S-XRD for the deep-drawn cups (2.0 DR) of A-SS, TRIP, D-SS, and D-TRIP, Fig. 8–10. For each cup, the PFs are measured at three different locations (i.e., RD, 45°, and TD locations) around the circumference of the cup at the rim (Fig. 1). The RD-ND-TD coordinates of the as-received alloy plate and the axial-radial-hoop coordinates of the deep-drawn cup are shown in the PFs. The scale bar shows texture intensity in terms of the multiples of random distribution (mrd).

4.3.1. fcc austenite texture in the A-SS cup

Fig. 8 presents the PFs of the austenite phase in the deep-drawn A-SS cup in comparison to the PFs of the as-received plate (blank). The ideal fcc texture components are summarized in Table 3 and also shown in Fig. 8 as a reference. The initial plate texture exhibits a relatively weak

Table 3
Ideal fcc texture components and their orientation relations with respect to the rolled plate axes. The plane normal of {hkl} is parallel to the normal direction (ND) and the <uvw> is parallel to the rolling direction (RD) of the alloy plate.

FCC components		{hkl} <uvw></uvw>
Cube, C		{001}<100>
Goss, G	\triangle	{110}<001>
Brass, Bs	\Diamond	{110}<112>
A	0	{110}<111>
Rotated Goss, Rt-G	∇	{110}<011>
Copper, Cu	+	{112}<111>

recrystallization texture with Cube {001}<100>, Brass {110}<112>, Goss {110}<001>, and Copper {112}<111> components as previously reported in [37]. At the RD location of the A-SS cup (the second row of Fig. 8), a strong <110> fiber texture formed along the radial direction of the cup (i.e., ND of the plate). Also, both <111> and <100> components are prominent along the axial direction of the cup (i.e., RD of the plate at the RD location), while the initial Cube component has diminished. At the 45° and TD locations, the main texture components are the same with <110>//radial and <111><100>//axial although the six-fold symmetry observed at RD is not as clear at these locations. Also, the subtle effect of initial blank texture is visible. For example, the <100>//axial is stronger at the TD location compared to the other two locations due to the relatively stronger initial intensity along TD in the blank. The opposite is true for the case of <111> intensity.

The deep-drawing texture of the A-SS cup near the rim is distinctly different from the rolling or tensile textures due to the complex strain path involving hoop compression, radial compression, axial tension, bending, and unbending. For example, the main difference compared to the tensile deformation texture is that <111> and <100> fiber textures are not prominent. The current result is consistent with the observation of the texture development in aluminum alloy cups by Savoie et al., where the final stable texture components are Goss $\{011\}<100>_D$ and P_D $\{011\}<111>_D$ [62]. The radial compression (blank holding compression associated with the ironing of thickened flange), the hoop and radial bi-compression along with rolling-like processing, and the axial tension along the drawing axis could be partly responsible for the development of $\{011\}//$ radial//ND, <110> six-fold symmetry components, and <111><100>//axial, respectively.

4.3.2. fcc and bcc textures in the TRIP cup

The fcc texture in the TRIP alloy blank (Fig. 9a) is slightly weaker but almost identical to that of the A-SS blank (Fig. 8). Also, the fcc PFs of the TRIP cup are qualitatively similar to those of the A-SS cup, in particular at the TD location, but weaker in the intensity. Moreover, the fcc texture is relatively isotropic around the rim of the TRIP cup. For the bcc α ' phase in the TRIP cup, (222), (110), and (200) PFs are presented in Fig. 9b. The Kurdjumov-Sachs (K-S) orientation relationship between the austenite and martensite phases is evident in that the correlations of $\{111\}\gamma$ // $\{110\}\alpha$ ' and $\langle110\rangle\gamma$ // $\langle111\rangle\alpha$ ' are clearly observed in Fig. 9a,b. It is expected that the martensite texture is predominantly transformation texture inherited from the austenite deformation texture during the deep-drawing process [19,21,22,63].

In terms of the dominant texture component in the martensite phase, <222> is the strongest between the axial and radial directions at all locations around the cup. In the fcc austenite, the shear plane and direction are $\{111\}$ and $\{110\}$, respectively. Upon bending of the alloy plate during the deep drawing process, fcc $\{110\}$ shear direction would be aligned between the axial and radial directions. This would cause bcc $\{111\}$ to intensify along the same orientation during the formation of transformation texture and result in a strong bcc $\{111\}$ texture component between the axial and radial (//ND) directions as observed at all three locations around the TRIP cup. Moreover, bcc $\{110\}$ intensity development along the axial direction correlates with the tensile texture

Р. Ноц. Ү. Li, W. Zhang et al. Materialia 18 (2021) 101162

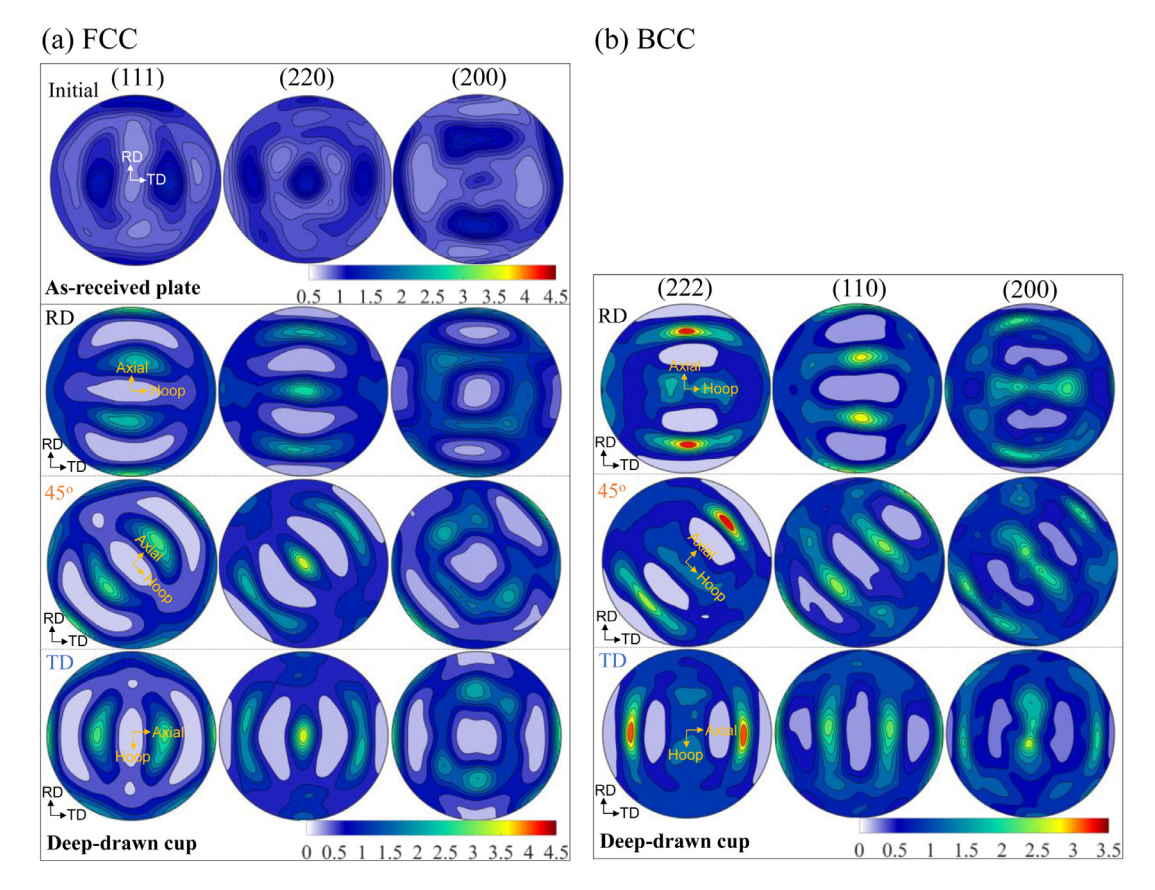


Fig. 9. Texture of TRIP cup (2.0 DR): PFs of (a) fcc austenite and (b) strain-induced bcc α ' martensite measured at RD, 45°, and TD locations (Fig. 1). Both RD-ND-TD and the axial-radial-hoop coordinates are presented. Also, the PFs of the fcc austenite phase in the as-received plate are presented as a reference.

components of fcc <111> and <100> along the axial direction. On the other hand, bcc <200> intensity development between hoop and radial directions may be due to the hoop and radial bi-compression, which is consistent with a corresponding depletion of fcc <200> along the radial and hoop orientations around the rim. Finally, the α ' martensite texture components and their intensities in the TRIP cup is relatively isotropic from RD to TD, which is consistent with the textures observed in the parent austenite phase. However, the maximum intensities of <111> and <220> of the α ' martensite phase are slightly higher at the RD location (3.44 and 3.04 mrd, respectively) compared to the TD location (3.34 and 2.42 mrd, respectively), even though the difference is relatively small.

4.3.3. fcc and bcc textures in the D-SS and D-TRIP cups

The deep-drawing texture of the D-SS cup is shown in Fig. 10a,b along with the initial texture. The as-received blank exhibits a characteristic texture of a rolled duplex steel. The fcc austenite exhibits a relatively strong Brass (with weak Goss, A, and Copper), whereas the bcc ferrite shows a strong Rotated-Cube with a partial α fiber [37]. The fcc PFs for the D-SS cup at RD (Fig. 10a) are quite similar to those of the A-SS cup with the same dominant components identified earlier. This suggests that the presence of the ferrite phase in the D-SS did not influence the development of austenite deformation texture during the deep drawing unlike the case of the TRIP cup where the in situ formation of martensite phase seems to have influenced the austenite texture development. Comparing the RD, 45°, and TD locations in the D-SS cup (Fig. 10a), the fcc (220) intensity along the radial direction (//ND) decreases noticeably, while it was more isotropic in the A-SS cup. The effect of the initial texture on the variations in the <111> and <200> axial intensities around the rim are also observed as it was in the A-SS cup.

In the D-SS cup (Fig. 10b), the ferrite texture is generally stronger than the austenite texture. The K-S relationship observed between the ferrite and austenite in the as-received D-SS blank is clearly maintained in the D-SS cup both in terms of the orientation relationships and intensity distributions around the cup (Fig. 10a,b). This is because the compression along radial direction (ND) would enhance fcc (220) and bcc (222), while the axial tension would intensify fcc (111) and bcc (110) along the drawing axis.

The fcc and bcc PFs in the D-TRIP cup (Fig. 10c,d) are qualitatively the same as those of D-SS cup, while the overall intensity (in particular for the bcc PFs) is weaker in the D-TRIP cup. It should be noted that for the case of bcc texture in the D-TRIP cup, the PFs present convoluted data from both the ferrite phase and strain-induced martensite phase. Comparing the PFs of the D-TRIP and D-SS cups, it is speculated that the ferrite deformation texture dominates the bcc PF intensities of the D-TRIP with little influence from the transformation texture in the relatively smaller amount of the martensite phase.

4.4. Distribution of phase stresses in the deep-drawn cups

Both hoop and axial residual stresses in constituent phases are measured using S-XRD for all four cups through the wall thickness and also along the wall height at the RD location. Note that, according to the FEM analysis, the radial and shear residual stresses were negligible from 50% to 100% of the cup wall height in all cases and, hence, the planestress assumption used in the stress calculation using the measured S-XRD strains (section 2.2) is reasonable.

4.4.1. Hoop residual stress

The hoop residual stress distributions in the deep-drawn cups are presented in Fig. 11. First, the residual stress profiles measured from the

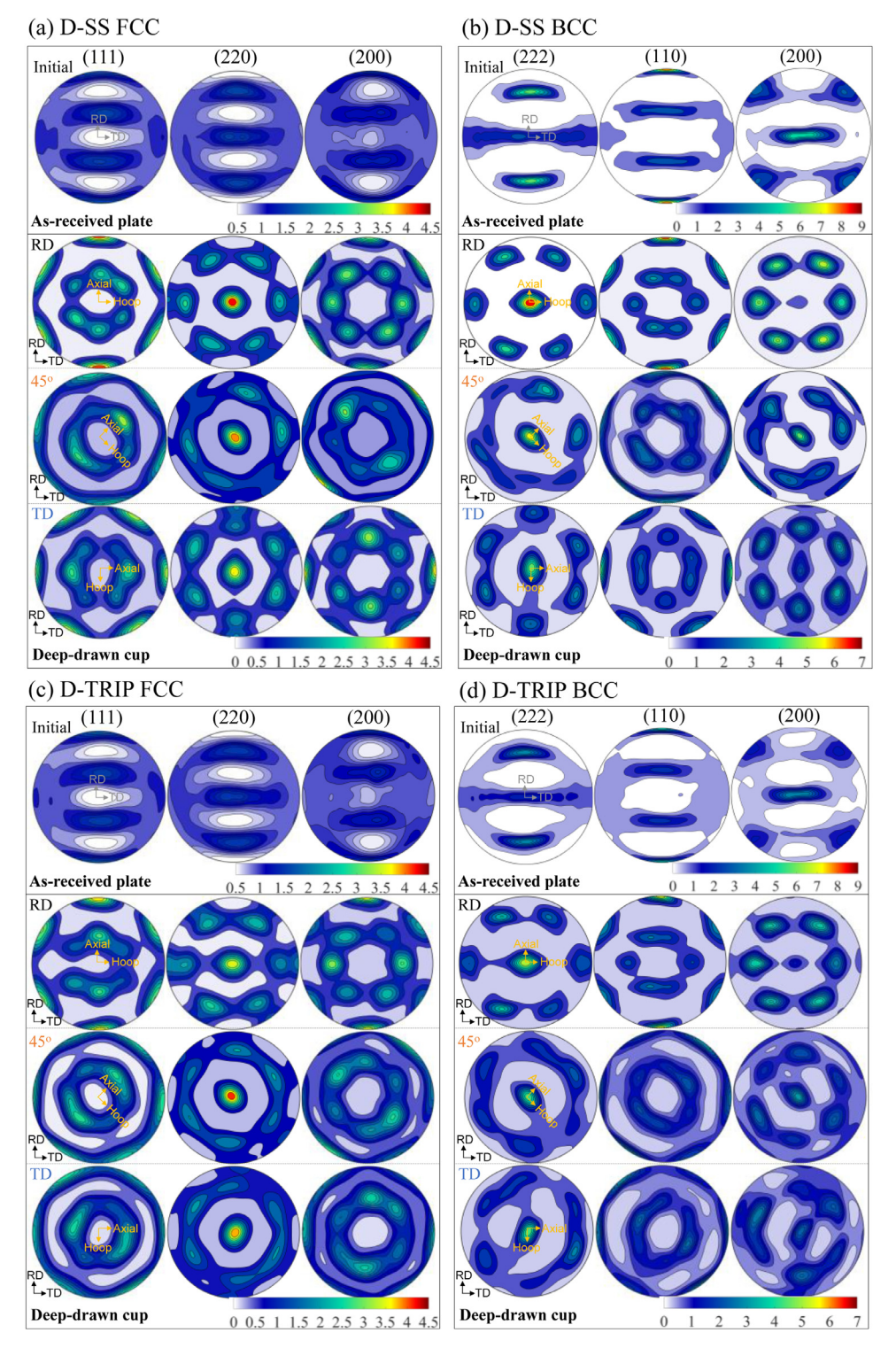


Fig. 10. Texture of D-SS and D-TRIP cups (2.0 DR). PFs of D-SS cup are presented for (a) fcc austenite and (b) bcc ferrite. PFs of D-TRIP cup are presented for (c) fcc austenite and (d) bcc phases of ferrite and strain-induced α ' martensite. The PF sets are presented for RD, 45°, and TD locations with both RD-ND-TD and the axial-radial-hoop coordinates. The reference PFs of as-received alloy plates are also presented.

single-phase A-SS cup provide the baseline understanding of the macroscopic residual stress distributions (i.e., Type 1 stress) in the deep-drawn cups. The S-XRD measured (symbols) and FEM calculated (lines) residual stresses in the A-SS cup are presented in Fig. 11b. At 99% of the wall height (i.e., near the rim), the hoop residual stress is tensile (about 690 MPa) at 0.5 mm from the outside surface of the cup wall. The tensile residual stress decreases gradually and becomes compressive at about 1.7 mm from the outside surface. The calculated stress from FEM agrees quite well with the measured data predicting a large tensile hoop residual stress at the outside surface. From 90% to 54% of the height, the

through-thickness hoop stress profiles are quite similar to each other with a much pronounced and symmetric transition from the tensile to compressive stress at about 1.1 mm from the outside surface. Nevertheless, the maximum tensile stress near the outside surface remains relatively constant along the height of the wall. Overall, the FEM results agrees well with the measured data, also clearly showing the difference between the profile at the rim (99% height) and the profiles below 90% of the wall height.

In the TRIP cup (Fig. 11a), the influence of the α ' formation during the deep drawing on the phase-specific residual stress partitioning

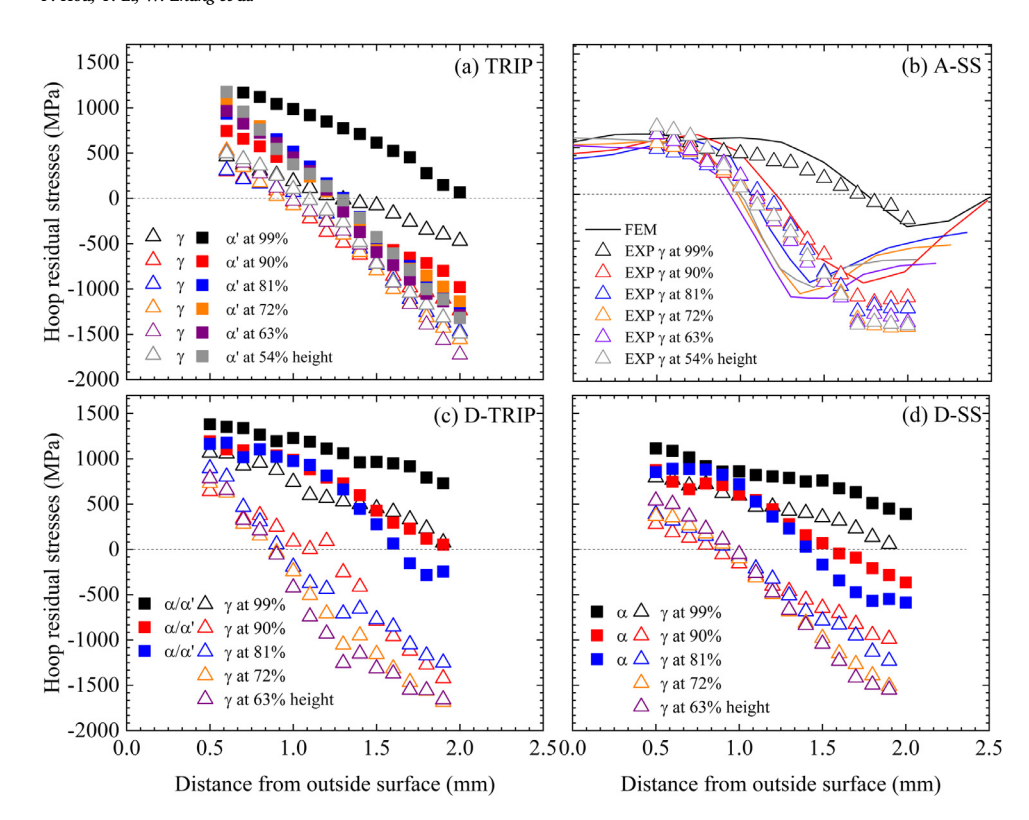


Fig. 11. Phase-specific hoop residual stresses measured as a function of the throughthickness distance from the outside surface (0 mm) into the inside surface of the deep-drawn cup wall. The through-thickness mapping was repeated as a function of the cup wall height from near the rim (99% height) to the midheight (e.g., 54% height). The S-XRD measurements were conducted at the RD location of the cup with 1.9 DR. (a) TRIP cup: austenite and strain-induced α 'martensite phases. (b) A-SS cup: austenite phase. The FEM calculated residual stresses are also presented for A-SS (lines). (c) D-TRIP cup: austenite and ferrite/martensite phases. (d) D-SS cup: austenite and ferrite phases.

is evident. As a result, while the austenite phase stresses in the TRIP are qualitatively similar to those in the A-SS, the overall stress profile is pushed downwards (towards less tensile and more compressive). In contrast, significant tensile hoop residual stresses concentrate in the α ' phase near the outside surface of the cup wall. For example, at 0.6 mm from the outside surface near the rim (99% height), the hoop residual stresses in the austenite and martensite phases are about 465 MPa and 1,150 MPa, respectively.

Similarly, in the D-SS cup (Fig. 11d), the ferrite phase bears more tensile hoop residual stress than the austenite phase at all measurement locations. Comparison of the hoop stresses in the D-TRIP and D-SS cups (Fig. 11c,d) shows that the bcc phases (i.e., convoluted ferrite and martensite data) in the D-TRIP cup show slightly higher hoop residual stresses than the ferrite phase at corresponding locations in the D-SS cup, while the austenite phase stresses are comparable. This suggests that the martensitic phase transformation has a measurable effect on the hoop residual stresses in the ferrite phase but has a limited effect on the austenite phase stress in the D-TRIP cup. The implications of the concentration of tensile hoop residual stresses in the α phase in the TRIP cup and the effectiveness of the ferrite phase on a stress redistribution in the D-TRIP cup will be discussed using the CPFEM results in section 5.1.

4.4.2. Axial residual stress

The axial stress profiles through the thickness of the A-SS cup (Fig. 12b) show a similar trend as the hoop residual stresses. Generally, the axial stresses are tensile near the outside surface and become compressive beyond the mid-thickness of the wall. However, the axial stresses at the rim (99% height) are quite relaxed. In fact, the measured tensile axial stress near the outside surface (0.5 mm) gradually increases along the height from the rim to the mid-height of the wall, reaching the maximum tensile stress of 810 MPa at 54% of the height. The numerical results of the FEM simulation agree well with the measured axial stresses in the A-SS cup (Fig. 12b). The macroscopic axial residual stress distribution shows that the highest tensile stress is at the outside surface at the middle of the cup height unlike the hoop stress distribution for which the maximum was observed near the rim.

Similarly, the tensile axial stress concentration in the α ' phase in the TRIP cup is negligible at the rim, Fig. 12a. Instead, as expected from the macroscopic axial stress distribution observed in the A-SS, the maximum tensile stress partitioned in the martensite phase (about 1,350 MPa) is observed near the mid-height of the cup wall. Also, the tensile axial stresses in the bcc phase(s) increases towards the mid-height of the cup in the D-TRIP and D-SS cases (Fig. 12c,d).

5. Discussion

5.1. Role of α 'and ferrite phases in the phase stress partitioning

5.1.1. Concentration of tensile stresses in the α ' phase in the TRIP cup

It is evident that the α ' phase forms in the TRIP and D-TRIP cups during the deep-drawing process according to the S-XRD analyses, Fig. 6,7. Consistent with the previous uniaxial tensile deformation studies of the same alloys [37], the metastable austenite phase in the TRIP cup partially transformed to ε and α' martensite phases, while only α' phase formed in the D-TRIP cup, Fig. 6. These strain-induced martensite phases influence the phase-specific stress partitioning during the deformation and often result in a stress concentration in the α' phase [20,37,41,64,65]. However, it has also been reported that the hcp ε martensite phase, which forms at shear band intersections and provides nucleation sites for the bcc α ' martensite phase [66], would not sustain a substantial load during plastic deformation, whereas the α ' martensite phase has a significant effect on the load partitioning behavior [20,37]. In the current study, the influence of the ε phase on the phase stress partitioning is not considered as a key factor responsible for the stress concentration in the deep-drawn TRIP cup.

As shown in Fig. 11a and Fig. 12a, the tensile hoop and axial residual stresses are indeed concentrated in the α ' phase in the TRIP cup at the outer surface of the cup wall. Accordingly, both hoop and axial stresses in the austenite phase in the TRIP cup show an overall decrease (less tensile) compared to those in the A-SS cup. This is expected because the macroscopic residual stress would transfer from the austenite matrix phase to the in situ forming α ' phase during the deep-drawing process.

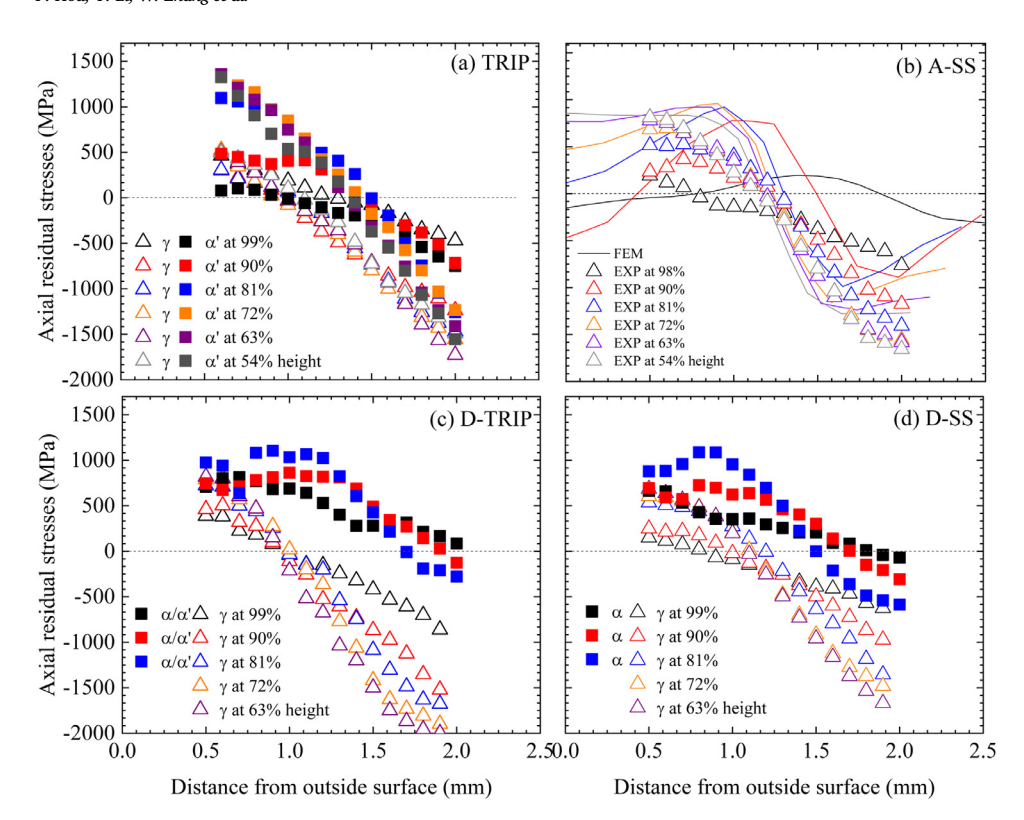


Fig. 12. The phase-specific axial residual stresses measured as a function of the through-thickness distance from the outside surface (0 mm) into the inside surface of the deep-drawn cup wall. The through-thickness mapping was repeated as a function of the cup wall height from near the rim (99% height) to the midheight (e.g., 54% height). The S-XRD measurements were conducted at the RD location of the cup with 1.9 DR. (a) TRIP, (b) A-SS (FEM calculated residual stresses are also presented), (c) D-TRIP, and (d) D-SS.

The cracks observed in the TRIP cup (Fig. 4) typically initiated at the outer surface at the rim, and then propagated through the wall thickness and vertically along the height. It has been observed that cracks typically nucleate within the α ' martensite region due to the local tensile-stress concentration, and propagate perpendicular to the tensile residual stress axes [67–70]. Moreover, the plastic strain accumulation at the crack-tip zone could further promote the martensitic phase transformation caused by the interactions of shear bands, deformation twins, or ϵ martensite [71]. The martensite-phase regions thus are further extended and such repeated nucleation and coalescence of α ' martensite promote the crack propagation in the TRIP cup. Therefore, the large tensile hoop stress development in the α ' phase at the outer surface of the rim could be a critical factor contributing to the cracking phenomenon observed in the TRIP cup.

5.1.2. Role of ferrite phase in load sharing in D-SS and D-TRIP cups

The effect of the ferrite in the load sharing in the D-SS cup was clearly displayed in Fig. 11d and Fig. 12d. The ferrite phase is the tensile load bearing phase in this duplex alloy, similar to the α ' phase in the TRIP. However, the tensile hoop stresses in the austenite is much closer to those in the ferrite in the D-SS unlike the larger partitioning between the austenite and martensite in the TRIP. According to the lattice strains measured using in-situ neutron diffraction during tensile deformation [37], the applied stress initially transfers from the plastically "soft" austenite to a "harder" ferrite at yielding in the D-SS alloy. As the applied stress increases further, the ferrite begins to deform plastically, resulting in the load transferring back to the strain-hardened austenite. As a result of such back and forth in the plastically-deforming vs. load-bearing roles, the difference in the residual lattice stresses in the austenite and ferrite phases after a large plastic deformation is not as significant in the D-SS alloy, compared to the residual stresses in the plastically-deforming austenite and non-deforming martensite phase in a TRIP alloy.

Although the tensile hoop residual stress in the bcc phases is higher in the D-TRIP cup (Fig. 11c) compared to the hoop stress in the α ' phase in the TRIP cup (Fig. 11a), the D-TRIP cup did not display any cracks

(Fig. 4). It should be noted that the two bcc phases (α ' martensite and the α ferrite) in the D-TRIP cup were not distinguishable in the highresolution S-XRD patterns due to their similar lattice parameters. Hence, the measured stresses in the bcc phases in the D-TRIP are convoluted as mentioned earlier (Fig. 11c) and the individual contributions of the α ' martensite and α ferrite phases to the overall residual stresses are difficult to discern experimentally. Therefore, to understand the role of the ferrite phase in the residual stress redistribution in the D-TRIP cup, the sequential-coupled CPFEM simulation was performed for both TRIP and D-TRIP cups, Fig. 13. Note that the measured α ' phase fraction in the TRIP cup (e.g., at the RD location) is about 24 wt.% (38 vol.%) at the rim at the outer surface, which would vary along the thickness and height of the cup. The S-XRD measured hoop residual strain data reflect such microstructural variations as presented in Fig. 11a. However, simulations of the in-situ formation of martensite phase and its spatial variation during a deep-drawing process using the CPFEM is beyond the scope of the current study. Instead, our goal is to use the CPFEM simulation with a given α ' phase fraction (e.g., 10 vol.%) in the D-TRIP* cup (Table 2b) to qualitatively assess the role of the ferrite phase in the D-TRIP* cup in the redistribution of the hoop stresses between the austenite, α' , and the ferrite phases.

First, the through-thickness profile of the hoop residual stress at the rim of the TRIP* cup is presented in comparison to that of A-SS in Fig. 13a. The tensile hoop residual stresses concentrate in the α ' martensite at the outer surface of the TRIP* cup, while the stress in the austenite phase is hardly affected, which is consistent with the S-XRD results. In the D-SS cup (Fig. 13b), the stress partitioning between the austenite and ferrite is also consistent with the S-XRD results a in that the ferrite phase in the duplex alloy is the tensile stress bearing phase at the outer surface. More importantly, in the D-TRIP* cup (Fig. 13b), the ferrite phase exhibits the largest tensile hoop residual stress instead of the martensite phase. Comparison between the TRIP* and D-TRIP* clearly shows that the addition of the ferrite phase resulted in a significant relaxation of the tensile hoop stress in the α ' phase as the tensile stress concentrates in the ferrite phase.

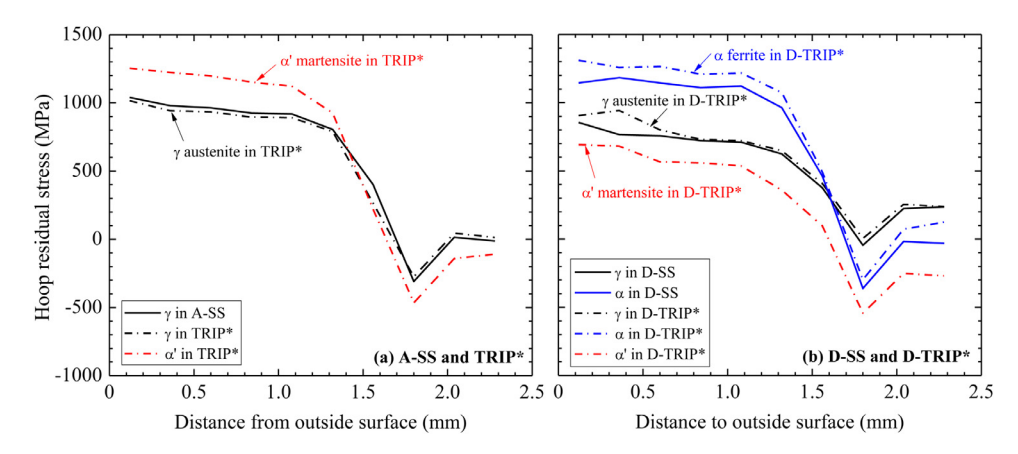


Fig. 13. Through-thickness profiles of the phase-specific hoop residual stresses at the rim calculated using the CPFEM simulation. (a) Stress partitioning between the austenite and α ' martensite phases in the TRIP* cup with the austenite stress in the A-SS cup as a reference. (b) Stress portioning between the austenite, α ferrite, and α ' martensite phases in the D-TRIP* cup with the austenite and ferrite stresses in the D-SS cup as references. For the TRIP* and D-TRIP* cases shown here, the α ' martensite phase fraction is 10 vol.% (Table 2b).

The current alloy design effort to improve the formability of a TRIP steel, while keeping the alloy composition cost-effective with a muchreduced Ni content, led to the development of the D-TRIP alloy, which indeed displayed a better resistance to the cracking phenomenon than the TRIP alloy. The CPFEM results show that the tensile hoop stresses in the brittle α ' in the deep-drawn TRIP cup can be significantly reduced in the D-TRIP cup by allowing the ductile ferrite phase to take a significant portion of the tensile stress, resulting in a better resistance to the cracking in the D-TRIP cup. Nevertheless, α' phase in the D-TRIP cup still accumulates a significant level of tensile hoop residual stress. Hence, when the deep drawing is performed at higher DRs (than 2.1 for the current study), the D-TRIP cup could become susceptible to cracking. However, it should be noted that, in addition to the reduction in the tensile load partitioning in the α ' phase, the refined ferrite and austenite grains in the D-TRIP alloy [37] could also contribute to the enhanced formability with increased grain and phase boundaries that act as microstructural barriers hindering the crack propagation even under more severe drawing conditions [70]. Also, the cracking behavior is strongly correlated to the α ' martensite phase fraction since a higher amount of α ' martensite often results in the formation of a network structure promoting the crack propagation [25]. Therefore, the relatively lower amount of α ' in the D-TRIP cup (Fig. 7) would further contribute to the enhanced formability.

5.2. Correlation of texture with α ' formation and plastic anisotropy

The cracking behavior in the TRIP cup (Fig. 5) exhibited different crack propagation rates varying from RD to TD. As discussed earlier in section 4.1, such orientation-dependent cracking behavior could be closely related to the variations in the α ' phase fraction around the rim of the TRIP cup (Fig. 7). In turn, the martensitic phase transformation kinetics and the variant selections could be strongly influenced by the texture of the parent austenite phase [19,21,63,72].

One of the strain components relevant to the variation in the martensitic phase transformation at the rim during the deep-drawing process is the circumferential compression acting on the sheet flange along the hoop direction [73]. Therefore, the α ' formation in the TRIP and D-TRIP cups could strongly correlate with the hoop compression along austenite <100>, according to the Bain model for the crystallographic orientation relationship between the austenite and α ' phases [74]. The Bain transformation would result in a weakening of austenite <100> and a strengthening of martensite <100> along the hoop direction. Indeed, the inverse pole figure (IPF) of the α ' phase in the TRIP cup (Fig. 14a) shows a development of strong <100> component along the hoop direction, which is a manifestation of a selective transformation texture rather than a compressive deformation texture [22,75]. Accordingly, the IPF of the austenite phase shows a complete depletion of <100> along the hoop direction, Fig. 14b. The preferential weakening of <100> is

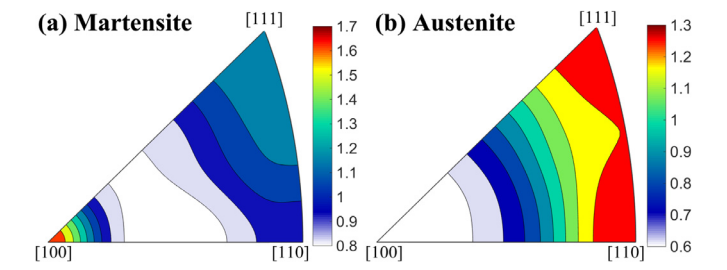


Fig. 14. Inverse pole figures of the TRIP cup (2.0 DR) measured at the RD location of the rim along the hoop direction. (a) Strain-induced α ' martensite phase and (b) austenite phase.

consistent with the selective martensitic transformation since a compressive deformation texture along the hoop direction would typically result in the weakening of both <111> and <100> components.

Similarly, the heterogenous distribution of the α ' martensite phase fraction around the rim of the deep-drawn cup could be rationalized by the initial austenite <100> intensity distribution along the hoop direction in the as-received alloy plate, Fig. 15. Note that the direction of the hoop compression at the RD location is along TD, and vice versa. The comparison shows that the changes in the α ' martensite phase fraction from RD to TD correlate reasonably well with the initial austenite <100> intensity distributions in both TRIP and D-TRIP cases. This suggests a plausible effect of the initial austenite texture on the α ' phase distribution in the deep-drawn cups, and, in turn, the orientation-dependent cracking behavior, especially in the TRIP cup.

Fig. 15b also shows a discrepancy between the martensite phase fraction and the austenite <100> intensity at around 45° location of the D-TRIP cup. This indicates that the distribution of the α ' phase in the D-TRIP cup may not be solely influenced by the initial austenite texture. In general, the relatively strong initial texture of the lamellar ferrite phase could result in a significant plastic anisotropy in cold-rolled duplex stainless steel alloys [76]. For instance, Moverare et al. [77] reported that the cold-rolled duplex stainless steel alloy exhibits a lower tensile strength when the loading direction is along 45°. In the current study, it was shown in Fig. 10 that the texture intensity in the ferrite phase varies significantly from RD to TD in the D-TRIP cup, which could contribute to the plastic anisotropy. Accordingly, the stress partitioning between the ferrite and austenite phases could vary from RD to TD. Our recent in-situ neutron diffraction study showed that the stresses in the ferrite phase decrease when the duplex alloy is subjected to a tensile loading along 45° due to higher Schmid factors for the ferrite grains [37]. This, in turn, resulted in an increase in the stress partitioning in the austenite phase along 45°, leading to an increase in the amount of α ' phase along this direction.

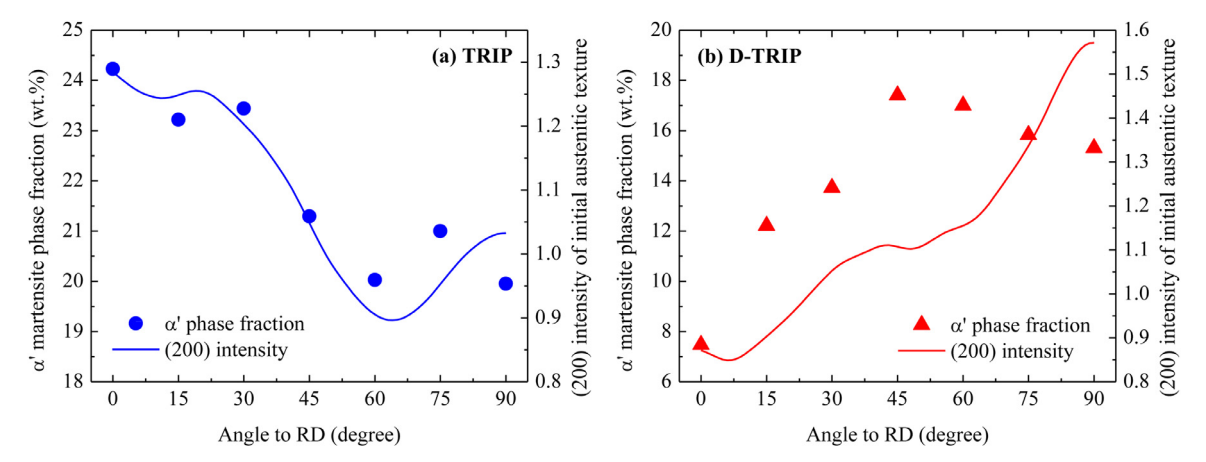


Fig. 15. Comparison of the circumferential distribution of the strain-induced α 'martensite phase fraction measured at various locations around the rim of the deep-drawn cups and the initial austenite <100> intensity along the hoop direction measured from the as-received plates from RD to TD. (a) TRIP and (b) D-TRIP.

6. Conclusions

The convoluted interplay among the constituent phases, martensitic phase transformation, crystallographic texture, and phase-specific residual stress partitioning was studied systematically to understand the mechanisms responsible for the cracking behavior and the formability of TRIP-assisted stainless steel (SS) alloys during a deep-drawing process at ambient temperature. Two key alloys were studied, namely TRIP and duplex TRIP (D-TRIP), along with their stable counterparts of austenitic steel (A-SS) and a duplex steel (D-SS) alloys. The microstructure, texture, and residual stress distributions in the deep-drawn cups were characterized using high-energy synchrotron x-ray diffraction (S-XRD) technique. Furthermore, the residual stress distribution in the deep-drawn cups were simulated using a crystal plasticity finite element modeling (CPFEM) scheme. In summary, the strain-induced martensitic phase transformation in the TRIP alloy results in a significant tensile stress development in the α ' martensite phase, making it susceptible to the cracking phenomenon during the deep-drawing process at ambient temperature. The stress partitioning behavior was optimized by introducing the ferrite phase in the D-TRIP alloy. By suppressing the development of a large tensile residual stresses in the α ' phase and also by lowering the overall amount of the α ' fraction, a better formability was observed in the D-TRIP alloy. The specific conclusions are as follows.

- The cracking phenomenon was observed in the TRIP cup processed with 1.9, 2.0, and 2.1 drawing ratios (DR), whereas the D-TRIP cup showed a good resistance to cracking. Also, the TRIP cup (2.1 DR) exhibited orientation-dependent cracking behavior. Along the rolling direction (RD) of the plate, the cracks propagated the longest and most rapidly.
- The strain-induced formation of martensite phases was observed in the TRIP and D-TRIP alloys during the deep-drawing process. The resulting microstructure of the TRIP cup consisted of retained austenite, ϵ martensite (hcp), and α ' martensite (bcc). In contrast, the D-TRIP cup consisted of the ferrite, retained austenite, and the α ' martensite. The α ' martensite phase fraction in the TRIP cup was slightly higher along the RD and was overall higher than the D-TRIP cup. Although the amount of α ' was smaller in the D-TRIP cup, the distribution was more anisotropic in that the variation around the circumference was more significant.
- The tensile hoop residual stress was concentrated in the brittle α' phase in the TRIP cup at the outer surface of the rim, which was responsible for the severe cracking problem observed. In the D-TRIP cup, the tensile hoop stress was concentrated in the ductile ferrite phase, and the tensile stress on the α' martensite was significantly reduced compared to the TRIP cup. The role of ferrite phase in the

- residual stress redistribution in the D-TRIP cup was critical for the improved formability of the D-TRIP compared to the TRIP case.
- Both TRIP and D-TRIP cups exhibited inhomogeneous distributions of α' phase around the circumference of the rim due to the nonuniform plastic deformation during the deep-drawing process. The initial austenite <100> intensity along the hoop direction in the alloy plates was correlated to the heterogeneous martensite phase fraction. In particular, for the TRIP cup, the variation in the α' martensite phase fractions around the rim, which correlates well with the orientation-dependent cracking behavior, was mostly attributed to the initial austenite <100> intensity distribution along the hoop direction. On the other hand, for the D-TRIP cup, the texture of the ferrite phase and corresponding plastic anisotropy seemed to have played an important role in the heterogenous martensite phase distribution as well.

Declaration of Competing Interest

The authors declare that they have no known competing financial interests or personal relationships that could have appeared to influence the work reported in this paper.

Acknowledgements

This research was partially funded by the U.S. National Science Foundation (NSF) Metals and Metallic Nanostructures (MMN) program under contract DMR-1308548 and DMR-1809640. This research was also supported in part by POSCO Corp., South Korea. P. Hou and H. Choo acknowledge funding from the State of Tennessee and Tennessee Higher Education Commission (THEC) through their support of the Center for Materials Processing at the University of Tennessee (UT). This research used resources of the Advanced Photon Source, a U.S. Department of Energy (DOE) Office of Science User Facility operated for the DOE Office of Science by Argonne National Laboratory under Contract No. DE-AC02-06CH11357. This work is a part of the Ph.D. dissertation of P. Hou under the supervision of Prof. H. Choo at UT.

References

- A. Ghosh, The influence of strain hardening and strain-rate sensitivity on sheet metal forming, J. Eng. Mater. Technol. 99 (3) (1977) 264–274.
- [2] A. Korbel, P. Martin, Microstructural events of macroscopic strain localization in prestrained tensile specimens, Acta Metall. 36 (9) (1988) 2575–2586.
- [3] F. Ozturk, D. Lee, Experimental and numerical analysis of out-of-plane formability test, J. Mater. Process. Technol. 170 (1-2) (2005) 247–253.
- [4] J. Poirier, Shear localization and shear instability in materials in the ductile field, J. Struct. Geol. 2 (1-2) (1980) 135–142.

- [5] R. Stringfellow, D. Parks, G.B. Olson, A constitutive model for transformation plasticity accompanying strain-induced martensitic transformations in metastable austenitic steels. Acta Metall. Mater. 40 (7) (1992) 1703–1716.
- [6] S.P. Keeler, Determination of forming limits in automotive stampings, SAE Technical Paper, SAE Trans. (1965) 1–9.
- [7] G.M. Goodwin, Application of strain analysis to sheet metal forming problems in the press shop, SAE Trans. (1968) 380–387.
- [8] S.S. Hecker, Simple technique for determining forming limit curves, Sheet Metal Ind. 52 (11) (1975) 671–676.
- [9] M. Azrin, W.A. Backofen, The deformation and failure of a biaxially stretched sheet, Metall. Trans. 1 (10) (1970) 2857–2865.
- [10] R.W. Imlay, Correlation of the Jurassic formations of North America, exclusive of Canada, Geol. Soc. Am. Bull. 63 (9) (1952) 953–992.
- [11] T.B. Stoughton, A general forming limit criterion for sheet metal forming, Int. J. Mech. Sci. 42 (1) (2000) 1–27.
- Mech. Sci. 42 (1) (2000) 1–27.
 [12] S. Kim, H. Huh, H. Bok, M. Moon, Forming limit diagram of auto-body steel sheets for high-speed sheet metal forming, J. Mater. Process. Technol. 211 (5) (2011) 851–862.
- [13] K. Bandyopadhyay, S. Basak, S. Panda, P. Saha, Use of stress based forming limit diagram to predict formability in two-stage forming of tailor welded blanks, Mater. Des. 67 (2015) 558–570.
- [14] N. Park, H. Huh, S.J. Lim, Y. Lou, Y.S. Kang, M.H. Seo, Fracture-based forming limit criteria for anisotropic materials in sheet metal forming, Int. J. Plast. 96 (2017) 1–35.
- [15] C. Xie, E. Nakamachi, The effect of crystallographic textures on the formability of high-strength steel sheets, J. Mater. Process. Technol. 122 (1) (2002) 104–111.
- [16] A.K. Srivastava, G. Jha, N. Gope, S. Singh, Effect of heat treatment on microstructure and mechanical properties of cold rolled C-Mn-Si TRIP-aided steel, Mater. Charact. 57 (2) (2006) 127–135.
- [17] K. Yoshida, Y. Tadano, M. Kuroda, Improvement in formability of aluminum alloy sheet by enhancing geometrical hardening, Comput. Mater. Sci. 46 (2) (2009) 459–468
- [18] F. Djavanroodi, A. Derogar, Experimental and numerical evaluation of forming limit diagram for Ti6Al4V titanium and Al6061-T6 aluminum alloys sheets, Mater. Des. 31 (10) (2010) 4866–4875.
- [19] E. Cakmak, H. Choo, K. An, Y. Ren, A synchrotron X-ray diffraction study on the phase transformation kinetics and texture evolution of a TRIP steel subjected to torsional loading, Acta Mater. 60 (19) (2012) 6703–6713.
- [20] K. Tao, H. Choo, H. Li, B. Clausen, J.-E. Jin, Y.-K. Lee, Transformation-induced plasticity in an ultrafine-grained steel: An in situ neutron diffraction study, Appl. Phys. Lett. 90 (10) (2007) 101911.
- [21] K. Tao, D.W. Brown, S.C. Vogel, H. Choo, Texture evolution during strain-induced martensitic phase transformation in 304L stainless steel at a cryogenic temperature, Metall. Mater. Trans. A 37 (12) (2006) 3469–3475.
- [22] E. Cakmak, S.C. Vogel, H. Choo, Effect of martensitic phase transformation on the hardening behavior and texture evolution in a 304L stainless steel under compression at liquid nitrogen temperature, Mater. Sci. Eng.: A 589 (2014) 235–241.
- [23] S. Cheng, X.-L. Wang, Z. Feng, B. Clausen, H. Choo, P.K. Liaw, Probing the characteristic deformation behaviors of transformation-induced plasticity steels, Metall. Mater. Trans. A 39 (13) (2008) 3105.
- [24] S. Cheng, H. Choo, Y. Zhao, X.-L. Wang, Y. Zhu, Y. Wang, J. Almer, P. Liaw, J. Jin, Y.-K. Lee, High ductility of ultrafine-grained steel via phase transformation, J. Mater. Res. 23 (6) (2008) 1578–1586.
- [25] P. Jacques, Q. Furnemont, T. Pardoen, F. Delannay, On the role of martensitic transformation on damage and cracking resistance in TRIP-assisted multiphase steels, Acta Mater. 49 (1) (2001) 139–152.
- [26] M.R. Berrahmoune, S. Berveiller, K. Inal, E. Patoor, Delayed cracking in 301LN austenitic steel after deep drawing: Martensitic transformation and residual stress analysis, Mater. Sci. Eng.-Struct. Mater. Prop. Microstruct. Process. 438 (2006) 262-266
- [27] S. Papula, J. Talonen, H. Hänninen, Effect of residual stress and strain-induced α' -martensite on delayed cracking of metastable austenitic stainless steels, Metall. Mater. Trans. A 45 (3) (2014) 1238–1246.
- [28] S. Papula, J. Talonen, O. Todoshchenko, H. Hänninen, Effect of internal hydrogen on delayed cracking of metastable low-nickel austenitic stainless steels, Metall. Mater. Trans. A 45 (11) (2014) 5270–5279.
- [29] J. Kim, S. Hong, N. Anjabin, B. Park, S. Kim, K.-G. Chin, S. Lee, H. Kim, Dynamic strain aging of twinning-induced plasticity (TWIP) steel in tensile testing and deep drawing, Mater. Sci. Eng.: A 633 (2015) 136–143.
- [30] M. Daymond, C. Tomé, M. Bourke, Measured and predicted inter-granular strains in textured austenitic steel, Acta Mater. 48 (2) (2000) 553–564.
- [31] S. Hong, J. Lee, S. Lee, W. Woo, S.-K. Kim, H.S. Kim, Residual stress analysis in deep drawn twinning induced plasticity (TWIP) steels using neutron diffraction method, Metall. Mater. Trans. A 45 (4) (2014) 1953–1961.
- [32] S. Papula, T. Sarikka, S. Anttila, J. Talonen, I. Virkkunen, H. Hänninen, Hydrogen-Induced Delayed Cracking in TRIP-Aided Lean-Alloyed Ferritic-Austenitic Stainless Steels, Materials 10 (6) (2017) 613.
- [33] A. Zinbi, A. Bouchou, Delayed cracking in 301 austenitic steel after bending process: martensitic transformation and hydrogen embrittlement analysis, Eng. Fail. Anal. 17 (5) (2010) 1028–1037.
- [34] W.-Y. Chu, J. Yao, C.-M. Hsiao, Hydrogen induced slow crack growth in stable austenitic stainless steels, Metall. Trans. A 15 (4) (1984) 729–733.
- [35] X. Guo, J. Post, M. Groen, W. Bleck, Stress oriented delayed cracking induced by dynamic martensitic transformation in meta-stable austenitic stainless steels, Steel Res. Int. 82 (1) (2011) 6–13.
- [36] S.H. Jung, T. Lee, S.W. Song, Y.J. Kwon, H.-G. Kang, D. Chae, C.S. Lee, Enhanced resistance to delayed cracking in deep-drawn lean duplex stainless steel: the role of residual stress, Korean J. Metals Mater. 55 (8) (2017) 544–549.

[37] P. Hou, Y. Li, D. Chae, Y. Ren, K. An, H. Choo, Lean duplex TRIP steel: Role of ferrite in the texture development, plastic anisotropy, martensitic transformation kinetics, and stress partitioning. Materialia 15 (2021) 100952.

- [38] P. Hou, Cracking and Earing Phenomenon in Deep-Drawn Stainless Steel Alloys: Role of Transformation Kinetics, Microstructure, and Texture, PhD Dissertation, University of Tennessee, Knoxville, 2020.
- [39] O. Muránsky, P. Šittner, J. Zrník, E. Oliver, In situ neutron diffraction investigation of the collaborative deformation–transformation mechanism in TRIP-assisted steels at room and elevated temperatures, Acta Mater. 56 (14) (2008) 3367–3379.
- [40] S. Harjo, Y. Tomota, P. Lukáš, D. Neov, M. Vrána, P. Mikula, M. Ono, In situ neutron diffraction study of α-γ Fe-Cr-Ni alloys under tensile deformation, Acta Mater. 49 (13) (2001) 2471–2479.
- [41] Y. Tomota, H. Tokuda, Y. Adachi, M. Wakita, N. Minakawa, A. Moriai, Y. Morii, Tensile behavior of TRIP-aided multi-phase steels studied by in situ neutron diffraction, Acta Mater. 52 (20) (2004) 5737–5745.
- [42] Y. Tomota, M. Ojima, S. Harjo, W. Gong, S. Sato, T. Ungár, Dislocation densities and inter-granular stresses of plastically deformed austenitic steels, Mater. Sci. Eng.: A 743 (2019) 32–39.
- [43] S. Harjo, N. Tsuchida, J. Abe, W. Gong, Martensite phase stress and the strengthening mechanism in TRIP steel by neutron diffraction, Sci. Rep. 7 (1) (2017) 1–11.
- [44] K. Tao, J.J. Wall, H. Li, D.W. Brown, S.C. Vogel, H. Choo, In situ neutron diffraction study of grain-orientation-dependent phase transformation in 304L stainless steel at a cryogenic temperature, J. Appl. Phys. 100 (12) (2006) 123515.
- [45] E. Cakmak, H. Choo, J.-Y. Kang, Y. Ren, Relationships between the phase transformation kinetics, texture evolution, and microstructure development in a 304L stainless steel under biaxial loading conditions: synchrotron X-ray and electron backscatter diffraction studies, Metall. Mater. Trans. A 46 (5) (2015) 1860–1877.
- [46] T. Gnaeupel-Herold, H.J. Prask, R.J. Fields, T.J. Foecke, Z.C. Xia, U. Lienert, A synchrotron study of residual stresses in a Al6022 deep drawn cup, Mater. Sci. Eng.: A 366 (1) (2004) 104–113.
- [47] E. Jimenez-Melero, N.H. van Dijk, L. Zhao, J. Sietsma, J.P. Wright, S. van der Zwaag, In situ synchrotron study on the interplay between martensite formation, texture evolution and load partitioning in low-alloyed TRIP steels, Mater. Sci. Eng.: A 528 (21) (2011) 6407–6416.
- [48] S. Cheng, Y.D. Wang, H. Choo, X.L. Wang, J.D. Almer, P.K. Liaw, Y.K. Lee, An assessment of the contributing factors to the superior properties of a nanostructured steel using in situ high-energy X-ray diffraction, Acta Mater. 58 (7) (2010) 2419–2429.
- [49] E. Jimenez-Melero, N. Van Dijk, L. Zhao, J. Sietsma, J. Wright, S. Van der Zwaag, In situ synchrotron study on the interplay between martensite formation, texture evolution and load partitioning in low-alloyed TRIP steels, Mater. Sci. Eng.: A 528 (21) (2011) 6407–6416.
- [50] A. Hammersley, FIT2D: an introduction and overview, Eur. Synch. Radiat. Facility Intern. Rep. ESRF97HA02T 68 (1997) 58.
- [51] L. Lutterotti, S. Matthies, H.-R. Wenk, A. Schultz, J. Richardson Jr, Combined texture and structure analysis of deformed limestone from time-of-flight neutron diffraction spectra, J. Appl. Phys. 81 (2) (1997) 594–600.
- [52] H. Wenk, K. Pawlik, J. Pospiech, J. Kallend, Deconvolution of superposed pole figures by discrete ODF methods: comparison of ADC and WIMV for quartz and calcite with trigonal crystal and triclinic specimen symmetry, Text., Stress, Microstruct. 22 (4) (1994) 233–260.
- [53] F. Bachmann, R. Hielscher, H. Schaeben, Texture analysis with MTEX-free and open source software toolbox, Solid State Phenomena, Trans. Tech. Publ. (2010) 63–68.
- [54] J.-S. Park, U. Lienert, P.R. Dawson, M.P. Miller, Quantifying three-dimensional residual stress distributions using spatially-resolved diffraction measurements and finite element based data reduction, Exp. Mech. 53 (9) (2013) 1491–1507.
- [55] A.S. Gill, Z. Zhou, U. Lienert, J. Almer, D.F. Lahrman, S. Mannava, D. Qian, V.K. Vasudevan, High spatial resolution, high energy synchrotron x-ray diffraction characterization of residual strains and stresses in laser shock peened Inconel 718SPF alloy, J. Appl. Phys. 111 (8) (2012) 084904.
- [56] B.H. Toby, R.B. Von Dreele, GSAS-II: the genesis of a modern open-source all purpose crystallography software package, J. Appl. Crystallogr. 46 (2) (2013) 544–549.
- [57] E. Kröner, Berechnung der elastischen Konstanten des Vielkristalls aus den Konstanten des Einkristalls, Zeitschrift für Physik 151 (4) (1958) 504–518.
- [58] Y. Huang, A User-Material Subroutine Incoroporating Single Crystal Plasticity in the ABAQUS Finite Element Program, Harvard Univ., 1991.
- [59] A. Needleman, R. Asaro, J. Lemonds, D. Peirce, Finite element analysis of crystalline solids, Comput. Meth. Appl. Mech. Eng. 52 (1-3) (1985) 689–708.
- [60] D. Peirce, R.J. Asaro, A. Needleman, Material rate dependence and localized deformation in crystalline solids, Acta Metall. 31 (12) (1983) 1951–1976.
- [61] Y. Gao, B. Larson, J. Lee, L. Nicola, J. Tischler, G. Pharr, Lattice rotation patterns and strain gradient effects in face-centered-cubic single crystals under spherical indentation, J. Appl. Mech. 82 (6) (2015).
- [62] J. Savoie, Y. Zhou, J.J. Jonas, S.R. Macewen, Textures induced by tension and deep drawing in aluminum sheets, Acta Mater. 44 (2) (1996) 587–605.
- [63] P. Hilkhuijsen, H.J.M. Geijselaers, T.C. Bor, E.S. Perdahcıoğlu, A.H. vd Boogaard, R. Akkerman, Strain direction dependency of martensitic transformation in austenitic stainless steels: the effect of γ-texture, Mater. Sci. Eng.: A 573 (2013) 100–105.
- [64] C. Pu, Y. Gao, Crystal plasticity analysis of stress partitioning mechanisms and their microstructural dependence in advanced steels, J. Appl. Mech. 82 (3) (2015) 031003.
- [65] X. Wu, M. Yang, F. Yuan, L. Chen, Y. Zhu, Combining gradient structure and TRIP effect to produce austenite stainless steel with high strength and ductility, Acta Mater. 112 (2016) 337–346.
- [66] G. Olson, M. Cohen, Kinetics of strain-induced martensitic nucleation, Metall. Trans. A 6 (4) (1975) 791.

[67] Y. Ogawa, S. Okazaki, O. Takakuwa, H. Matsunaga, The roles of internal and external hydrogen in the deformation and fracture processes at the fatigue crack tip zone of metastable austenitic stainless steels, Scr. Mater. 157 (2018) 95–99.

- [68] K.S. Choi, W.N. Liu, X. Sun, M.A. Khaleel, Microstructure-based constitutive modeling of TRIP steel: Prediction of ductility and failure modes under different loading conditions, Acta Mater. 57 (8) (2009) 2592–2604.
- [69] A. Matsushita, S. Ueki, Y. Mine, K. Takashima, Comparative Study of Microstructure-sensitive Fatigue Crack Propagation in Coarse-and Fine-grained Microstructures between Stable and Metastable Austenitic Stainless Steels Using Miniature Specimen, ISIJ Int. (2021) 659 ISIJINT-2020-.
- [70] J. Stolarz, N. Baffie, T. Magnin, Fatigue short crack behavior in metastable austenitic stainless steels with different grain sizes, Mater. Sci. Eng.: A 319-321 (2001) 521–526
- [71] G.B. Olson, M. Cohen, A general mechanism of martensitic nucleation: Part I. general concepts and the FCC→ HCP transformation, Metall. Trans. A 7 (12) (1976) 1897–1904.

- [72] M. Humbert, B. Petit, B. Bolle, N. Gey, Analysis of the γ-ε-α' variant selection induced by 10% plastic deformation in 304 stainless steel at 60°C, Mater. Sci. Eng.: A 454 (2007) 508–517.
- [73] D. Daniel, J. Savoie, J. Jonas, Textures induced by tension and deep drawing in low carbon and extra low carbon steel sheets, Acta Metall. Mater. 41 (6) (1993) 1905–1920.
- [74] E.C. Bain, N. Dunkirk, The nature of martensite, trans. AIME 70 (1) (1924) 25–47.
- [75] L. Toth, J. Jonas, D. Daniel, R. Ray, Development of ferrite rolling textures in low-and extra low-carbon steels, Metall. Trans. A 21 (11) (1990) 2985–3000.
- [76] N. Jia, R.L. Peng, Y. Wang, S. Johansson, P. Liaw, Micromechanical behavior and texture evolution of duplex stainless steel studied by neutron diffraction and selfconsistent modeling, Acta Mater. 56 (4) (2008) 782–793.
- [77] J.J. Moverare, M. Oden, Influence of elastic and plastic anisotropy on the flow behavior in a duplex stainless steel, Metall. Mater. Trans. A 33 (1) (2002) 57–71.